Article

Directly imaging the cooling flow in the Phoenix cluster

https://doi.org/10.1038/s41586-024-08369-x

Received: 25 June 2024

Accepted: 8 November 2024

Published online: 5 February 2025

Check for updates

Michael Reefe[1]✉, Michael McDonald[1], Marios Chatzikos[2], Jerome Seebeck[3], Richard Mushotzky[3], Sylvain Veilleux[3], Steven W. Allen[4,5,6], Matthew Bayliss[7], Michael Calzadilla[1,8], Rebecca Canning[9], Benjamin Floyd[10], Massimo Gaspari[11], Julie Hlavacek-Larrondo[12], Brian McNamara[13], Helen Russell[14], Keren Sharon[15] & Taweewat Somboonpanyakul[16]

In the centres of many galaxy clusters, the hot (approximately 10^7 kelvin) intracluster medium can become dense enough that it should cool on short timescales[1,2]. However, the low measured star formation rates in massive central galaxies[3–6] and the absence of soft X-ray lines from the cooling gas[7–9] suggest that most of this gas never cools. This is known as the cooling flow problem. The latest observations suggest that black hole jets are maintaining the vast majority of gas at high temperatures[10–16]. A cooling flow has yet to be fully mapped through all the gas phases in any galaxy cluster. Here we present observations of the Phoenix cluster[17] using the James Webb Space Telescope to map the [Ne VI] λ 7.652-μm emission line, enabling us to probe the gas at $10^{5.5}$ kelvin on large scales. These data show extended [Ne VI] emission that is cospatial with the cooling peak in the intracluster medium, the coolest gas phases and the sites of active star formation. Taken together, these imply a recent episode of rapid cooling, causing a short-lived spike in the cooling rate, which we estimate to be 5,000–23,000 solar masses per year. These data provide a large-scale map of gas at temperatures between 10^5 kelvin and 10^6 kelvin in a cluster core, and highlight the critical role that black hole feedback has in not only regulating cooling but also promoting it[18].

In many galaxy clusters, the hot intracluster medium (ICM) in the inner regions (approximately 100 kpc) is dense and cool enough that it should rapidly cool and fuel a massive starburst in the central galaxy on timescales much shorter than the age of the Universe[1]. Such 'cooling flows' are largely absent, with observed star formation rates in central cluster galaxies rarely exceeding 1–10 $M_\odot\,\mathrm{yr}^{-1}$ (refs. 2–6). This implies the presence of energy sources that suppress the cooling, with the most likely being feedback from an active galactic nucleus (AGN). X-ray observations suggest that this is achieved by bipolar radio jets emitted from the AGN, which inject mechanical energy and drive turbulence in the surrounding ICM, as well as inflate large buoyant cavities or 'bubbles' of plasma that can transport low-entropy gas outwards[10–12,18,19]. Simulations modelling the underlying physics show that this feedback can be recurrently induced by the feeding of the supermassive black hole, for example, through thermally unstable cooling and cold gas precipitation, intrinsically linking the processes of feeding and feedback[13–16]. In this context, the Phoenix cluster[17,20] (redshift $z = 0.597$) is an outlier, as it seems to follow all of the original predictions for an uninhibited cooling flow. It has an enormous starburst[17], a massive cold gas reservoir[21], a rapidly accreting supermassive black hole powering an AGN in the central galaxy[20], a power-law entropy profile all the way into the core[20] and a central cooling time comparable to the free-fall time and considerably shorter than the turbulent eddy timescale (which measures the time for a turbulent vortex to oscillate and produce density fluctuations in the surrounding medium)[20,22].

Previous studies attempting to directly detect the cooling flow of the Phoenix cluster have yielded mixed results. Coronal emission lines, which probe gases at intermediate temperatures (10^5–10^6 K), provide a promising avenue for directly tracing cooling flows. Observations of the O VI $\lambda\lambda$ 1032, 1038 Å coronal-line doublet in the Phoenix cluster with the Cosmic Origins Spectrograph of the Hubble Space Telescope (HST) imply massive amounts of cooling (55,000 $M_\odot\,\mathrm{yr}^{-1}$) when assuming 100% of the observed flux is because of cooling[23]. However, these observations lack spatial information, making the source of the O VI emission ambiguous, and require a large, highly uncertain correction for intrinsic extinction in the far-ultraviolet regime. Observations of soft X-ray lines with the Reflection Grating Spectrometer of the X-ray Multi-Mirror Mission, on the other hand, reveal a cooling rate of

[1]Kavli Institute for Astrophsyics and Space Research, Massachusetts Institute of Technology, Cambridge, MA, USA. [2]Department of Physics and Astronomy, University of Kentucky, Lexington, KY, USA. [3]Department of Astronomy and Joint Space-Science Institute, University of Maryland, College Park, MD, USA. [4]Kavli Institute for Particle Astrophysics and Cosmology, Stanford University, Stanford, CA, USA. [5]Department of Physics, Stanford University, Stanford, CA, USA. [6]SLAC National Accelerator Laboratory, Menlo Park, CA, USA. [7]Department of Physics, University of Cincinnati, Cincinnati, OH, USA. [8]Center for Astrophysics, Harvard & Smithsonian, Cambridge, MA, USA. [9]Institute of Cosmology and Gravitation, University of Portsmouth, Portsmouth, UK. [10]Department of Physics and Astronomy, University of Missouri–Kansas City, Kansas City, MO, USA. [11]Department of Physics, Informatics and Mathematics, University of Modena and Reggio Emilia, Modena, Italy. [12]Département de Physique, Université de Montréal, Montréal, Québec, Canada. [13]Department of Physics and Astronomy, University of Waterloo, Waterloo, Ontario, Canada. [14]School of Physics and Astronomy, University of Nottingham, University Park, UK. [15]Department of Astronomy, University of Michigan, Ann Arbor, MI, USA. [16]Department of Physics, Faculty of Science, Chulalongkorn University, Bangkok, Thailand. ✉e-mail: mreefe@mit.edu

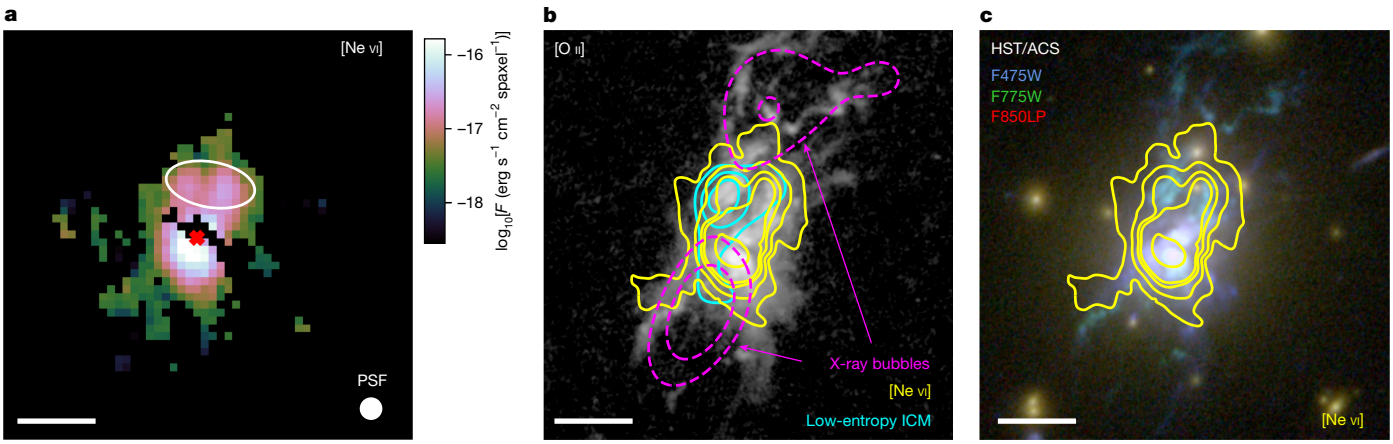

Fig. 1 | Maps of the [Ne VI]-emitting coronal gas in the central galaxy of the Phoenix cluster overlaid with the hotter and colder gas phases, and starlight. a, A two-dimensional map of the [Ne VI] λ 7.652-μm flux from channel 3 of the MIRI/MRS data. The flux is in $\log_{10}[F\,(\mathrm{erg\ s^{-1}\ cm^{-2}\ spaxel^{-1}})]$, where a channel-3 spaxel is 0.04 arcsec^2. The white ellipse shows the aperture that we use to capture the region of extended northern emission. A scale bar is provided in the bottom left, and the size of the point spread function (PSF) full-width at half-maximum is shown in the bottom right. The red cross marks the peak integrated brightness at 23 h 44 min 43.9157 s, −42° 43′ 12.3972″. Only spaxels in which the line is detected with signal-to-noise ratio (S/N) ≥ 3 are shown. **b**, An [O II] image of the central galaxy of the Phoenix cluster is shown in the greyscale using data from the HST Advanced Camera for Surveys (HST/ACS)[20]. The extended [O II] emission is indicative of ongoing star formation. The cyan contours show the entropy of the ICM, which decreases towards the centre of the cluster and reaches a minimum in the northeast cloud. The yellow contours show the flux of the [Ne VI] line (as shown in **a**), which is cospatial with the brightest [O II] and the lowest-entropy gas. The magenta dashed contours show the locations of the X-ray bubbles that are filled by radio jets, marking the location in which the X-ray emission is 2σ and 4σ below the mean[20]. **c**, A three-colour RGB image of the central galaxy of the Phoenix cluster is shown using data from the HST/ACS in the F475W, F775W and F850LP filters. The blue colours indicate young, actively forming stellar populations. The [Ne VI] contours from **b** are shown here as well, highlighting the spatial coincidence between the blue star-forming filaments and the cooling gas. Scale bars, 2.0″, 13 kpc.

$350^{+250}_{-200}\ M_\odot\ \mathrm{yr^{-1}}$ when fitting a combined isothermal gas and cooling flow model, which can barely sustain the 500–800 $M_\odot\ \mathrm{yr^{-1}}$ starburst[24]. Cooling rates measured with these methods often disagree: Far Ultraviolet Spectroscopic Explorer observations of Abell 1795, Abell 2597 and Perseus reveal O VI cooling rates higher than the X-ray rates[25,26]. Like the O VI line in the far-ultraviolet regime, soft X-rays may be obscured by cool, dusty clouds closely interleaved with the hot gas, causing the observed X-ray cooling rates to underpredict the amount of 'hidden' cooling gas[27]. By contrast, the lack of soft X-ray emission may be explained if coronal emission is produced by the heating and mixing of ambient cold gas with the hot atmosphere, rather than the cooling of the hot atmosphere itself. Observations of the C IV λ1549 Å line in the Virgo cluster[28,29] and the [Fe X] λ 6374 Å coronal line in the Centaurus cluster[30,31] seem to favour heating by thermal conduction or mixing compared with pure cooling flow models.

In this work, we present integral field unit (IFU) observations of the [Ne VI] λ 7.652-μm coronal line, which probes a similar temperature range as O VI (approximately $10^{5.5}$ K) but in a wavelength regime with effectively no extinction and no stellar continuum, using the Mid-Infrared Instrument of the James Webb Space Telescope (JWST) in the Medium Resolution Spectroscopy mode (referred to as MIRI/MRS). We develop a full mid-infrared spectral model to fit the continuum and emission lines in each 'spaxel' (a spatial pixel) of the IFU data, performing a simultaneous spectral and spatial deconvolution of the central, dust-obscured quasi-stellar object (QSO) and the larger-scale emission. A map of the QSO-subtracted [Ne VI] flux is shown in Fig. 1a. This map represents a marked improvement on previous observations of extended coronal emission[26,30], which have detected $10^{5.5}$ K gas in only a handful of spaxels. In the Phoenix cluster, we clearly detect [Ne VI] emission in hundreds of spaxels encompassing tens of kiloparsecs, enabling us to see coherent structure in the coronal phase for the first time, to our knowledge. This map clearly shows two clouds of roughly $10^{5.5}$ K gas to the north of the nucleus, cospatial with the minimum entropy of the hot atmosphere[20], the low- and high-ionization optical emission lines[32], the cold molecular gas[21] and a region of enhanced star formation (Fig. 1). A one-dimensional radial intensity profile reveals that the [Ne VI] emission is consistent with a large-scale diffuse nebula that is being photoionized by the central QSO and a localized cooling region with a size of ≤5 kpc at a distance of approximately 10 kpc from the nucleus (Fig. 2). In principle, this bump in the radial profile could be caused by a local increase in the gas density (n_e). However, we detect a similar bump in the [Ne VI]/[Ne V] ratio, which is insensitive to n_e, in the same region. Taken together, this implies a local change in the dominant ionization mechanism, such as from AGN photoionization to cooling. The presence of a cloud with an effective temperature nearly 30 times less than the lowest temperature seen in the X-ray-emitting ICM and nearly 30 times higher than the optical line emitting gas lying directly beneath the buoyantly rising X-ray bubble could be related to either uplifting of low-entropy gas from the core[18,19,33] and/or rapid cooling driven in situ by turbulence[34], both of which can be explained by the AGN feedback model. In the latter case, turbulent motions result from compressions, rarefactions and stretching in the surrounding medium, which can be induced by AGN jets, winds and shocks from the bubble[35].

The total [Ne VI] flux in this cloud north of the nucleus (Fig. 1, white ellipse) is $4.9^{+0.5}_{-0.7} \times 10^{-16}$ erg s^{-1} cm^{-2}, which alone is enough to imply an unphysical cooling rate of >100,000 $M_\odot\ \mathrm{yr^{-1}}$, motivating a more complex two-component model. We model the mid-infrared spectrum using Cloudy[36,37] assuming that the emission is because of a combination of a central ionizing source and a cooling parcel of gas. The cooling gas starts with an initial density of $n_e = 0.42\ \mathrm{cm^{-3}}$, temperature $kT = 2.3$ keV and metallicity $Z = 0.55 Z_\odot$, based on the X-ray data at the location of the extended [Ne VI] gas[20]. It cools until it reaches the temperatures of the interstellar medium (10^4 K). Metal abundances are measured using high-resolution X-ray spectroscopy of the central region of the cluster[24] that have been recomputed for this work. While cooling, the gas is exposed to radiation from the central AGN. Moreover, although the central AGN in the Phoenix cluster is highly obscured along our line of sight, it is probably unobscured, or considerably less obscured, from the perspective of the cooling gas, as this gas lies along the jet axis in which the AGN will not be obscured by the dusty torus. We adopt a generic spectral energy distribution template constructed from a recent sample of hyperluminous quasars[38] and rescale it to a

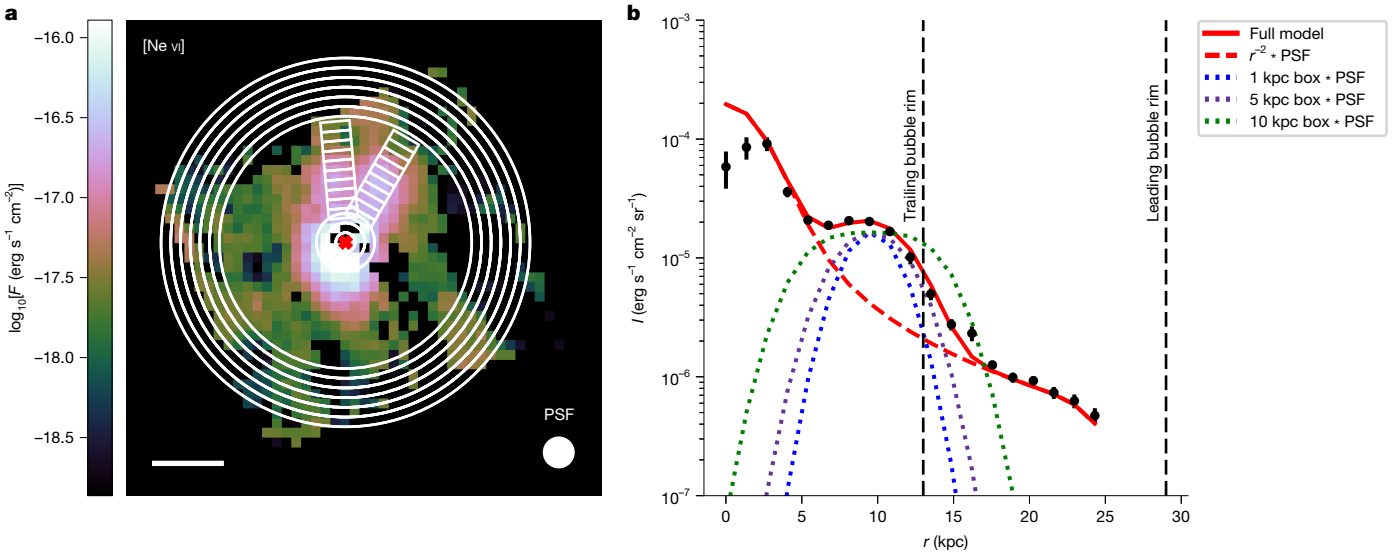

Fig. 2 | A radial surface brightness profile of the northern [Ne VI] emission in the central galaxy of the Phoenix cluster. a, A two-dimensional map of the [Ne VI] flux. Here only spaxels with S/N ≥ 1 are shown. A series of rectangular apertures are shown in white, which span from the nucleus out to 25 kpc in 2 directions aligned with the northern clouds of emission. The innermost and outermost apertures are circular annuli to improve the statistics. Scale bar, 1.5″, 10 kpc. **b**, A collapsed one-dimensional intensity (*I*) surface brightness profile is shown in which measurements are taken by an average and standard deviation of the spaxels in each aperture. The profiles in the two directions shown in **a** are averaged to create the final one-dimensional profile. The dashed red line shows an r^{-2} power law convolved with the instrumental PSF, and the dotted lines show box functions with different widths in different colours, also convolved with the PSF. The asterisks indicate convolution. The solid red line is the combined model using a box width of 5 kpc. The edges of the X-ray bubble are also annotated by vertical dashed lines at 13 kpc and 29 kpc. The prominent bump in the profile that deviates from an r^{-2} power law is coincident with the northern emission region beneath the bubble, and has a size of ≲5 kpc.

bolometric luminosity of 3×10^{47} erg s^{-1}, matching that of the Phoenix cluster[17]. Cosmic rays are also included, with a background ionization rate of 2×10^{-16} s^{-1} (ref. 39).

The net effect of AGN radiation is to lower the inferred cooling rates of the lines. Photoionization injects energy into the gas and increases the population of ions that contribute to the line luminosities, which increases the inferred luminosity per unit mass of cooling gas. The sound-crossing time of the low-entropy gas of approximately 10 Myr is comparable to the cooling time in the same region, both shorter than the cloud collapse time of around 75 Myr. Therefore, the cooling probably proceeds at some intermediate rate between the isobaric and isochoric predictions[40]. Enabling a combination of these two modes and factoring in the photoionization from the central AGN, we obtain a nominal cooling rate for the [Ne VI] line of 25,000 ± 5,000 $M_\odot$ yr^{-1}, for which this uncertainty is purely statistical. When we consider all high-ionization lines in the spectrum ([Ne VI], [Ne V], [Fe VIII], [Fe VII], [Mg VII] and O VI), the average cooling rate is 10,000 ± 5,000 $M_\odot$ yr^{-1} (the uncertainty listed here is the median absolute deviation of the individual cooling rates). Indeed, the cooling rates of all the infrared lines are of a similar magnitude (Fig. 3a), indicating that our model describes the overall spectrum reasonably well across the wide variety of ionization states of the infrared lines (Extended Data Table 1). The O VI line is an outlier, most probably owing to uncertainties in the ultraviolet extinction correction. We explore the effects of varying the bolometric luminosity of the quasar and the hot-phase abundance of neon, which (aside from the measured line fluxes) are the dominant drivers of the inferred cooling rates. We perform additional simulations adjusting these quantities to be higher or lower by a factor of two and find local scaling relations between the recovered cooling rates and the varied quantities for each line. Assuming the effects of the QSO luminosity and neon abundance combine multiplicatively and combining measurements for all the infrared coronal lines, we find a plausible range of cooling rates of 5,000–23,000 $M_\odot$ yr^{-1} at approximately $10^{5.5}$ K.

We also consider a set of more complex models in which gas from the hot 10^7 K ICM first mixes with the warm 10^4 K interstellar medium in different proportions, cooling the hot atmosphere non-radiatively. This mixed gas phase then cools radiatively down to 10^4 K as it is illuminated by the AGN, in the same manner as our unmixed models. The metal abundances in this model are treated as a mix of the ICM and interstellar medium abundances, with the latter including the depletion of refractory elements onto dust grains[41]. Supplementary Information provides more details. We find that these models are able to produce more consistent cooling rates and line ratios than the unmixed models (Fig. 3b). The average cooling rate is constrained to 15,000 ± 2,000 $M_\odot$ yr^{-1}, with a scatter 2.5 times lower than the unmixed model. The plausible range of cooling rates then becomes 7,000–36,000 $M_\odot$ yr^{-1}. We present these models as a promising alternative to the unmixed models and a showcase of how metal abundances, in particular, have a strong effect on the results, but we are cautious in claiming this scenario to be the underlying truth because of the additional systematic uncertainties introduced by the additional model parameters. However, it is apparent from the results of both models that whether the gas undergoes mixing or not, there is strong evidence for vast quantities of gas cooling through $10^{5.5}$ K in excess of 5,000 $M_\odot$ yr^{-1}.

Our most conservative estimate of the cooling rate (5,000–23,000 $M_\odot$ yr^{-1}) is significantly higher than the classical cooling rate inferred by the X-ray gas (approximately 3,800 $M_\odot$ yr^{-1}). However, the latter is based on the bolometric X-ray luminosity and is averaged over several gigayears, whereas the emission-line cooling measurements are nearly instantaneous. We propose that the high cooling rate, of the order of 10^4 $M_\odot$ yr^{-1} at temperatures of $10^{5.5}$ K, is short-lived and not representative of the long-term cooling rate of this cluster[42,43]. This cooling spike is unlikely to last much longer than the sound-crossing time of the bubble (approximately 10 Myr), forming 0.5×10^{11} $M_\odot$ to 2×10^{11} $M_\odot$ of molecular gas. This is a few times higher than the observed $2.1 \pm 0.3 \times 10^{10}$ $M_\odot$ (ref. 21), which could hint at large quantities of molecular gas being destroyed by feedback[27], or in the case of mixing, that some fraction of the gas is being prevented from cooling all the way down to the molecular phase by repeatedly remixing with the hot ICM. Our Cloudy modelling is in excellent agreement with

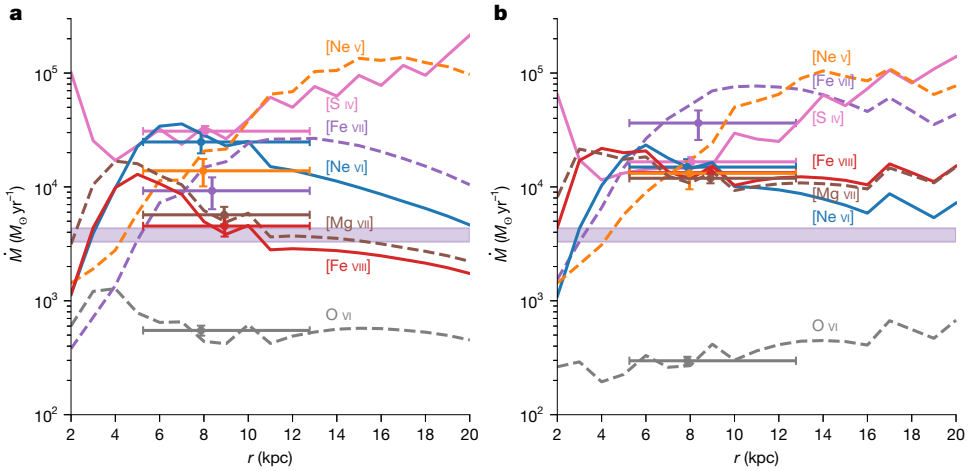

Fig. 3 | Cloudy-simulated cooling rates for a radiatively cooling parcel of gas that is being illuminated by a central AGN at various distances from the nucleus. a, Cooling rates $\dot{M}$ for each line are shown as a function of distance from the nucleus, assuming that all of the luminosity in the northern cloud is contained in a small Δr at each radius. The lines are coloured according to which emission line they correspond to. The intensity-weighted-average cooling rates in the northern cloud are plotted with error bars: the x errors show the extent of the northern cloud, the x locations of the points themselves are the intensity-weighted central radii and the y errors show the statistical 1σ uncertainties. The translucent purple band shows the inferred cooling rate from the X-ray emitting gas, which lies between the infrared lines and O VI. **b**, The same as in **a**, but showing the results for our simulations that considered the initial gas conditions to be in a mixing layer between the hot and warm phases.

all the observed line ratios, all of which are within a factor of a few of the model prediction. The only lines that disagree significantly are the low-ionization [Ne II] line (probably boosted considerably by star formation and weak shocks) and O VI line (again, probably owing to a highly uncertain extinction correction). We show the results for the cooling rates in Fig. 3 and the line ratios in Supplementary Fig. 3.

Finally, we consider the velocity profile of the [Ne VI]-emitting gas to further understand its origin. The coronal gas motions along our line of sight contain contributions from both bulk motions and turbulence imparted by the bubble, as evidenced by the large linewidths (full-width at half-maximum of about 1,000 km s^{-1}). Despite this, Fig. 4b shows that the velocity profile exhibits a coherent structure as a function of radius. We explore a toy model for the velocity profile of the cooling gas, considering the bulk motion imparted by the wake of a buoyantly rising bubble as it expands adiabatically in a stratified ICM[20]. This model adequately describes the data at small radii out to approximately 7 kpc,

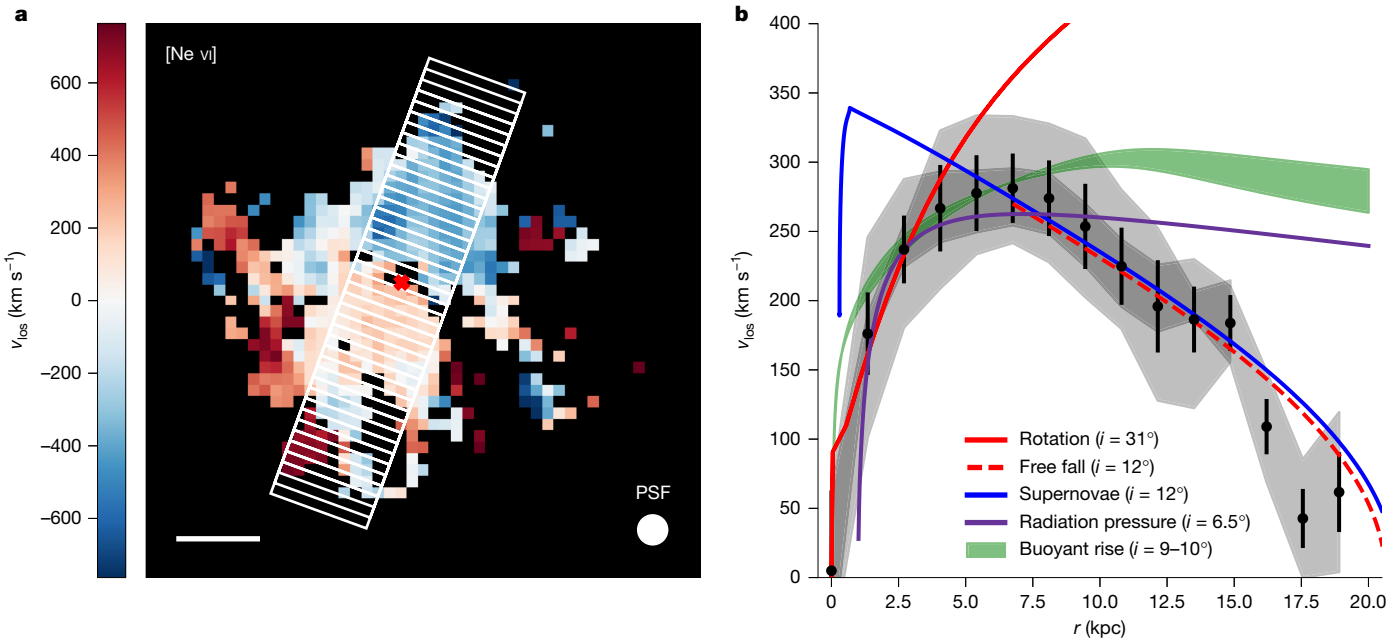

Fig. 4 | North–south velocity profile of the [Ne VI]-emitting gas in the central galaxy of the Phoenix cluster, overlaid with various models. **a**, A two-dimensional map of the median line-of-sight velocity of [Ne VI]. Here only spaxels in which [Ne VI] is detected with S/N ≥ 2 are shown. A series of rectangular apertures are shown in white, which span the vertical height of the central galaxy (from approximately −30 kpc to +30 kpc). Scale bar, 1.5″, 10 kpc. **b**, A collapsed one-dimensional velocity profile is shown in which measurements are taken by an S/N-weighted average and standard deviation of the spaxels in each aperture. The grey bands show the individual left-side and right-side velocity profiles, and the black data points show the average of these two profiles. A series of velocity models for pure rotation, ionized winds from supernovae, radiation pressure from the central AGN and a buoyantly rising bubble are overplotted with varying inclination angles to best match the observed profile.

at which point the gas may be slowing down because of its increased density relative to the ICM[44,45]. At radii larger than 7 kpc, the observed kinematics of the cooling gas are consistent with free fall. This suggests that the observed coronal emission may be attributed to low-entropy gas that has been lifted from the core. For reference, a number of other velocity models are shown. We also provide additional commentary on the morphology and kinematics of the coronal phase compared with the cooler gas phases in the Supplementary Information.

Although the ideas behind cooling flows date back to the first high-resolution images of galaxy clusters[1], they have largely remained undetected. This may be because AGN feedback is highly effective in moderating cooling[10,46], that episodes of pure cooling are common but short-lived[42,43] or because the majority of the cooling is obscured[27,47]. For the first time, to our knowledge, we have mapped all the phases of this cooling flow in both temperature and space, providing the most complete picture of cooling so far. In the core of the Phoenix cluster, we observe rapid cooling of the hot atmosphere, with traces of gas cascading through transitions in the ultraviolet, optical, infrared and millimetre. Critically, this cooling gas is cospatial with the lowest-entropy X-ray-emitting gas, lying directly behind a buoyantly rising bubble in the hot atmosphere, suggesting that the gas is cooling in the turbulent wake behind the bubble, perhaps stimulated by first mixing with the cooler gas. If short-lived cooling episodes are common in the galaxy cluster population, providing the necessary fuel for ongoing AGN feedback, then Phoenix provides a unique window into this critically important, but rarely captured, process for understanding the formation of the most massive galaxies in the Universe.

Online content

Any methods, additional references, Nature Portfolio reporting summaries, source data, extended data, supplementary information, acknowledgements, peer review information; details of author contributions and competing interests; and statements of data and code availability are available at https://doi.org/10.1038/s41586-024-08369-x.

1. Fabian, A. C., Nulsen, P. E. J. & Canizares, C. R. Cooling flows in clusters of galaxies. *Nature* **310**, 733–740 (1984).
2. Fabian, A. C. Cooling flows in clusters of galaxies. *Annu. Rev. Astron. Astrophys.* **32**, 277–318 (1994).
3. McNamara, B. R. & O'Connell, R. W. Star formation in cooling flows in clusters of galaxies. *Astron. J.* **98**, 2018–2043 (1989).
4. Allen, S. W. Starbursts in cooling flows: blue continua and emission-line nebulae in central cluster galaxies. *Mon. Not. R. Astron. Soc.* **276**, 947–960 (1995).
5. Hicks, A. K. & Mushotzky, R. Star formation rates in cooling flow clusters: a UV pilot study with archival XMM-Newton optical monitor data. *Astrophys. J. Lett.* **635**, L9–L12 (2005).
6. McDonald, M., Gaspari, M., McNamara, B. R. & Tremblay, G. R. Revisiting the cooling flow problem in galaxies, groups, and clusters of galaxies. *Astrophys. J.* **858**, 45 (2018).
7. Canizares, C. R., Markert, T. H. & Donahue, M. E. in *Cooling Flows in Clusters and Galaxies* (ed. Fabian, A. C.) 63 (1988).
8. David, L. P. et al. A high-resolution study of the Hydra A cluster with Chandra: comparison of the core mass distribution with theoretical predictions and evidence for feedback in the cooling flow. *Astrophys. J.* **557**, 546–559 (2001).
9. Peterson, J. R. et al. High-resolution X-ray spectroscopic constraints on cooling-flow models for clusters of galaxies. *Astrophys. J.* **590**, 207–224 (2003).
10. McNamara, B. R. & Nulsen, P. E. J. Heating hot atmospheres with active galactic nuclei. *Annu. Rev. Astron. Astrophys.* **45**, 117–175 (2007).
11. Fabian, A. C. Observational evidence of active galactic nuclei feedback. *Annu. Rev. Astron. Astrophys.* **50**, 455–489 (2012).
12. Hlavacek-Larrondo, J. et al. X-ray cavities in a sample of 83 SPT-selected clusters of galaxies: tracing the evolution of AGN feedback in clusters of galaxies out to z=1.2. *Astrophys. J.* **805**, 35 (2015).
13. Gaspari, M., Melioli, C., Brighenti, F. & D'Ercole, A. The dance of heating and cooling in galaxy clusters: three-dimensional simulations of self-regulated active galactic nuclei outflows. *Mon. Not. R. Astron. Soc.* **411**, 349–372 (2011).
14. Prasad, D., Sharma, P. & Babul, A. Cool core cycles: cold gas and AGN jet feedback in cluster cores. *Astrophys. J.* **811**, 108 (2015).
15. Li, Y., Ruszkowski, M. & Bryan, G. L. AGN heating in simulated cool-core clusters. *Astrophys. J.* **847**, 106 (2017).
16. Yang, H. Y. K., Gaspari, M. & Marlow, C. The impact of radio AGN bubble composition on the dynamics and thermal balance of the intracluster medium. *Astrophys. J.* **871**, 6 (2019).
17. McDonald, M. et al. A massive, cooling-flow-induced starburst in the core of a luminous cluster of galaxies. *Nature* **488**, 349–352 (2012).
18. McNamara, B. R. et al. A mechanism for stimulating AGN feedback by lifting gas in massive galaxies. *Astrophys. J.* **830**, 79 (2016).
19. Revaz, Y., Combes, F. & Salomé, P. Formation of cold filaments in cooling flow clusters. *Astron. Astrophys.* **477**, L33–L36 (2008).
20. McDonald, M. et al. Anatomy of a cooling flow: the feedback response to pure cooling in the core of the Phoenix cluster. *Astrophys. J.* **885**, 63 (2019).
21. Russell, H. R. et al. Alma observations of massive molecular gas filaments encasing radio bubbles in the Phoenix cluster. *Astrophys. J.* **836**, 130 (2017).
22. Gaspari, M. et al. Shaken snow globes: kinematic tracers of the multiphase condensation cascade in massive galaxies, groups, and clusters. *Astrophys. J.* **854**, 167 (2018).
23. McDonald, M. et al. Deep Chandra, HST-COS, and Megacam observations of the Phoenix cluster: extreme star formation and AGN feedback on hundred kiloparsec scales. *Astrophys. J.* **811**, 111 (2015).
24. Pinto, C. et al. AGN feedback in the Phoenix cluster. *Mon. Not. R. Astron. Soc.* **480**, 4113–4123 (2018).
25. Oegerle, W. R. et al. FUSE observations of cooling-flow gas in the galaxy clusters A1795 and A2597. *Astrophys. J.* **560**, 187–193 (2001).
26. Bregman, J. N., Fabian, A. C., Miller, E. D. & Irwin, J. A. On VI observations of galaxy clusters: evidence for modest cooling flows. *Astrophys. J.* **642**, 746–751 (2006).
27. Fabian, A. C. et al. Hidden cooling flows in clusters of galaxies. *Mon. Not. R. Astron. Soc.* **515**, 3336–3345 (2022).
28. Sparks, W. B. et al. Hundred thousand degree gas in the Virgo cluster of galaxies. *Astrophys. J. Lett.* **750**, L5 (2012).
29. Anderson, M. E. & Sunyaev, R. Searching for FUV line emission from 10^7K gas in massive elliptical galaxies and galaxy clusters as a tracer of turbulent velocities. *Mon. Not. R. Astron. Soc.* **459**, 2806–2821 (2016).
30. Canning, R. E. A. et al. Detection of optical coronal emission from 10^6-K gas in the core of the Centaurus cluster. *Mon. Not. R. Astron. Soc.* **411**, 411–421 (2011).
31. Chatzikos, M. et al. Implications of coronal line emission in NGC 4696*. *Mon. Not. R. Astron. Soc.* **446**, 1234–1244 (2015).
32. McDonald, M. et al. The state of the warm and cold gas in the extreme starburst at the core of the Phoenix galaxy cluster (SPT-CLJ2344-4243). *Astrophys. J.* **784**, 18 (2014).
33. Pope, E. C. D., Babul, A., Pavlovski, G., Bower, R. G. & Dotter, A. Mass transport by buoyant bubbles in galaxy clusters. *Mon. Not. R. Astron. Soc.* **406**, 2023–2037 (2010).
34. Gaspari, M., Ruszkowski, M. & Sharma, P. Cause and effect of feedback: multiphase gas in cluster cores heated by AGN jets. *Astrophys. J.* **746**, 94 (2012).
35. Wittor, D. & Gaspari, M. Dissecting the turbulent weather driven by mechanical AGN feedback. *Mon. Not. R. Astron. Soc.* **498**, 4983–5002 (2020).
36. Ferland, G. J. et al. CLOUDY 90: numerical simulation of plasmas and their spectra. *Publ. Astron. Soc. Pac.* **110**, 761–778 (1998).
37. Chatzikos, M. et al. The 2023 release of Cloudy. *Rev. Mex. Astron. Astrofis.* **59**, 327–343 (2023).
38. Saccheo, I. et al. The WISSH quasars project. XI. The mean spectral energy distribution and bolometric corrections of the most luminous quasars. *Astron. Astrophys.* **671**, A34 (2023).
39. Indriolo, N., Geballe, T. R., Oka, T. & McCall, B. J. H^+_3 in diffuse interstellar clouds: a tracer for the cosmic-ray ionization rate. *Astrophys. J.* **671**, 1736–1747 (2007).
40. Gaspari, M. Shaping the X-ray spectrum of galaxy clusters with AGN feedback and turbulence. *Mon. Not. R. Astron. Soc.* **451**, L60–L64 (2015).
41. Jenkins, E. B. A unified representation of gas-phase element depletions in the interstellar medium. *Astrophys. J.* **700**, 1299–1348 (2009).
42. Gaspari, M., Temi, P. & Brighenti, F. Raining on black holes and massive galaxies: the top-down multiphase condensation model. *Mon. Not. R. Astron. Soc.* **466**, 677–704 (2017).
43. Prasad, D., Sharma, P., Babul, A., Voit, G. M. & O'Shea, B. W. Cool-core cycles and Phoenix. *Mon. Not. R. Astron. Soc.* **495**, 594–599 (2020).
44. Fabian, A. C. et al. The relationship between the optical Hα filaments and the X-ray emission in the core of the Perseus cluster. *Mon. Not. R. Astron. Soc.* **344**, L48–L52 (2003).
45. Gendron-Marsolais, M. et al. Revealing the velocity structure of the filamentary nebula in NGC 1275 in its entirety. *Mon. Not. R. Astron. Soc.* **479**, L28–L33 (2018).
46. McNamara, B. R. & Nulsen, P. E. J. Mechanical feedback from active galactic nuclei in galaxies, groups and clusters. *New J. Phys.* **14**, 055023 (2012).
47. Fabian, A. C. et al. Hidden cooling flows in clusters of galaxies II: a wider sample. *Mon. Not. R. Astron. Soc.* **521**, 1794–1807 (2023).

Methods

Observations and data reduction

Data collection. We obtained mid-infrared IFU observations of Phoenix A using the MIRI/MRS instrument of the JWST as a part of the cycle 1 General Observer programme ID 2439. The on-source observations were taken from 15:44:52 UTC on 27 July 2023 to 02:32:02 UTC on 28 July 2023, and background observations were taken from 02:32:06 UTC to 04:48:42 UTC on 28 July 2023. These observations were taken in all the channels and all bands, which cover rest-frame wavelengths from 3.1 μm to 17.5 μm at $z = 0.597$. The SHORT-band exposure was 6.95 h, whereas the MEDIUM-band and LONG-band exposures were 51.0 min and 85.8 min, respectively. Note that the SHORT-band exposure was the longest because our primary goal was the detection of extended [Ne VI] emission, which falls in that band. Background exposures were 51.0 min, 16.8 min and 25.2 min, respectively. The on-source and background observations used the recommended four-point and two-point dither patterns. The field of view of each MIRI channel is shown in Extended Data Fig. 1 over an optical image.

The HST/ACS data (Fig. 1 and Extended Data Fig. 1) were obtained using programme ID 15315. Data were gathered in the broadband F475W, F775W and F850LP filters for two orbits, two orbits and one orbit, respectively, and in the narrowband FR601N filter centred on [O II] for eight orbits. Details for these data and data reduction are available elsewhere[20].

The ICM entropy and X-ray cavity data presented in Fig. 1 were modelled using data from Chandra Advanced CCD Imaging Spectrometer-I comprising a series of programmes with IDs of 13401, 16135, 16545, 19581, 19582, 19583, 20630, 20631, 20634, 20635, 20636 and 20797, totalling 551 ks of exposure time. Details on these data are available elsewhere[20].

Data reduction. We opt to reduce the data ourselves to enable the data reduction pipeline to be optimized for our observations, which are in a low-surface-brightness regime with deep exposures. We reduce the data using the JWST pipeline version 1.12.3 and CRDS context jwst_1140.pmap. We follow the default pipeline options for most of the data reduction, with a few exceptions. We increase the sensitivity for flagging jumps from cosmic ray showers, and we perform an additional cleaning routine that finds warm pixels using the corresponding background exposures, marking them in both background and science frames[48]. We enable the two-dimensional residual fringe correction step to suppress fringing on the individual spaxel level. Moreover, for the background subtraction step, we choose the option that directly subtracts a median-combined two-dimensional background exposure in a pixel-by-pixel manner from the science exposures. This is in contrast to the default pipeline option that creates a one-dimensional sigma-clipped background spectrum by combining all of the background spaxels at each wavelength and then subtract this from the data in each spaxel. The latter method has the advantage of introducing less noise into the background-subtracted data, but we have found that in our data, this leaves residual detector artefacts that are better removed by performing the two-dimensional background subtraction. We also produce cubes in the IFU-detector-aligned axes to enable a direct comparison with the point spread function (PSF). Supplementary Information provides more details on further refinements that we perform on the data.

Spectral models

Model decomposition. To model the spectra in each spaxel, we use a fitting code written in the Julia programming language[49]: Likelihood Optimization of gas Kinematics in IFUs (https://github.com/Michael-Reefe/Loki.jl). The total model can be summarized as

$$I_\nu(x,y,\lambda) = \left[\sum_{i=1}^{2} A_i^{\rm dust}\frac{B_\nu(\lambda,T_i)}{(\lambda/9.7)^2} + \sum_{j=1}^{N_{\rm PAH}} A_j^{\rm PAH} D_j(\lambda) + \sum_{k=1}^{N_{\rm line}} A_k^{\rm line} G_k(\lambda)\right] e^{-\tau(\lambda)} + A^{\rm QSO}(\lambda) I_\nu^{\rm QSO}(\lambda)\,{\rm PSF}(x,y,\lambda) \quad (1)$$

The first term represents thermal dust emission, where $B_\nu(\lambda, T_i)$ is the Planck function per unit frequency ν at temperature T_i, and we assume a dust emissivity that is $\propto 1/\lambda^2$. We fit two dust temperatures in the range of (35, 300) K, in which the upper limit is chosen to prevent fitting hotter dust temperatures that are presumably heated by the QSO. This limit is also consistent with that used by another work[50] in which PAHFIT software was used to fit the star-forming galaxies. The second term is the emission from polycyclic aromatic hydrocarbon (PAH) molecules, where $D_j(\lambda)$ is a Drude profile[51]. The central wavelengths and full-widths at half-maximum (FWHMs) of the Drude profiles are taken from the average values obtained from another work[52], which are updated for JWST based on the original values from PAHFIT. We also enable a small variation of ±0.05 μm for the centres and ±10% for the widths to account for the increased spectral resolution of MIRI compared with Spitzer. The third term is the gas emission lines, where $G_k(\lambda)$ is a Gaussian profile. Each line is enabled to be modelled by up to two Gaussian profiles (Supplementary Information). We correct the measured FWHMs using the FWHM of the line spread function[53]. The line-of-sight velocities are limited to ±800 km s^{-1}, and the FWHMs are limited to ≤1,500 km s^{-1}. We also tie the kinematics of lines with similar ionization potentials to represent different gas phases, ending up with four groups: molecular H_2, cool (ionization potential <24 eV), warm (24 < ionization potential < 90 eV) and coronal (ionization potential >90 eV). The wavelengths and ionization potentials of the fit coronal lines, plus [Ne II] and [S IV], are given in Extended Data Table 1. We assume a simple screen geometry such that the first three terms are extincted by a factor $e^{-\tau(\lambda)}$, where τ is the optical depth of silicate dust. We follow the methods of another work[54] to model $\tau(\lambda)$ by dividing the silicates into three species. We fix the relative abundances of these species based on a fit to the integrated spectrum from channels 1–4, because we find that enabling them to be free in each spaxel often leads to extinction compensating for residual instrument artefacts and producing unphysical results. The final term represents the contamination from the QSO spectrum that is present because of the PSF (Supplementary Information). $I_\nu^{\rm QSO}$ is taken as the spectrum of the brightest spaxel divided by the PSF model of the same spaxel. Normalization $A^{\rm QSO}(\lambda)$ is constant in each channel, but may be different between channels. This represents how far the QSO contribution is enabled to deviate from what is predicted purely from our PSF model, which we constrain in a factor of 2: (0.5, 2).

Modelling procedure. Our minimization procedure is subdivided into three stages.

1. Mask out the emission lines and fit the continuum. In this step, the PAHs are not fit with Drude profiles. Instead, they are modelled using two of the templates from ref. 50, as in ref. 55. This was done because the spectra have a relatively high optical depth and weak PAH features. Fitting everything simultaneously can, thus, lead to the spectral decomposition procedure confusing how much of the flux around the 9.7-μm silicate absorption feature is because of the broad wings of the surrounding PAH features versus the continuum and leading to unphysically large PAH fluxes.
2. Subtract the thermal dust continuum and QSO contribution obtained using step 1 above, mask out the emission lines and fit the PAHs to the residual spectrum using Drude profiles.
3. Mask out the emission lines, subtract the QSO template contribution and fit a cubic spline to the residuals with a spacing of 7 pixels between knots. Subtract this cubic spline fit and use the residuals to fit the emission lines. By subtracting a cubic spline fit instead of the fit obtained using the previous steps, we are able to obtain

accurate line fluxes even when the physically motivated continuum model under- or overpredicts the continuum locally around a line.

We use the Levenberg–Marquardt least squares minimization algorithm[56] for each step in the fitting process. However, for the emission-line fit in step 3, we use the simulated annealing global minimization algorithm as implemented by Optim.jl[57], for which results are then used as a starting point for the Levenberg–Marquardt minimization to refine the parameters.

To generate our results, we implement this procedure to fit in a spaxel-by-spaxel manner on a data cube containing the combined channel-3 data, and similarly for the channel-2 and channel-4 data (cutting out channel 4C because of low sensitivity). As the QSO PSF component outshines the host galaxy in many spaxels, this makes it difficult to measure the optical depth of the underlying host galaxy. As such, we have developed a technique to independently measure this based on the flux ratios of the rotational H_2 lines. The H_2 0–0 S(3) line lands near the peak of the 9.7-μm silicate absorption feature, whereas the S(4) line is unaffected. Therefore, we use the S(4)/S(3) line ratio as a proxy for the optical depth. We perform an initial fit to measure the observed H_2-line fluxes and then we fit excitation models to the upper-level column densities, masking out the S(3) line, to obtain an 'intrinsic' S(4)/S(3) line ratio. Comparing this with the observed line ratio gives us the optical depth, which we then use to run a second iteration of our fitting procedure. A more detailed description of this process is provided elsewhere (M.A.R. et al., manuscript in preparation). We also repeat all of these fits without including the QSO template component (substituting it for an additional thermal dust component that may be up to 1,500 K), to enable a comparison with the results for the QSO-subtracted maps. For regions of interest, such as the northern extended cloud and the nucleus, we create an integrated one-dimensional spectrum combining channels 2–4 (excluding channel 4C) and fit with 100 bootstrapping iterations. We also do this for the entire field of view of channel 2. Examples of one-dimensional spectral fits are shown in Extended Data Figs. 2 and 3. Two-dimensional maps of the fluxes, line-of-sight velocities and linewidths for [Ne VI], [Ne II] and [Ne V] are shown in Extended Data Figs. 4–9.

Surface brightness models

To create the radial surface brightness profile shown in Fig. 2, we use a series of rectangular apertures of 3 × 1 spaxels going from the nucleus through the two cooling clouds, and averaging these together. The outermost and innermost apertures become circular annuli to improve the statistics. We then model this profile by considering the case in which the entire [Ne VI] emission can be attributed to the central QSO, assuming a constant gas density and a consistent emitting cloud geometry. In this scenario, we would expect an inverse-square-law fall-off in the emission-line intensity. As shown in Fig. 2, there is a distinct bump that deviates away from the r^{-2} power law at a distance of approximately 5–13 kpc from the nucleus, corresponding to the emission region beneath the X-ray bubble (at almost 20 kpc). This bump could be explained by a local increase in n_e, because the [Ne VI] line emission, coming from collisional excitations, is proportional to $n_e n_{Ne^{5+}}$. However, the fact that we also see a bump in the [Ne VI]/[Ne V] ratio, which is insensitive to both n_e and metallicity, at the same location suggests that there is a local change in the ionization parameter ($U \equiv n_{\gamma,i}/n_H$, the ratio of the ionizing photon density to the hydrogen density) and thus the dominant ionization mechanism. To account for this, we add a second component to our model, representing the cloud as a simple boxcar function with varying position and width. Fitting this two-component model, we find the cloud to be centred at approximately 10 kpc and has a size along the radial direction of ≤5 kpc. Above this, the fit becomes significantly worse, as shown by the 10 kpc boxcar size in the figure. Note that this model has also been convolved with the instrumental PSF (assuming it is a Gaussian).

Cooling models

We assume that the coronal emission comes from ICM gas cooling to low temperatures. In our simulations, starting from the ICM density and temperature discussed in the main text, we let a unit-volume parcel of gas cool from the ambient temperature down to 10,000 K, and track its evolution assuming that it cools under either isobaric or isochoric conditions. We use version 23.00 of Cloudy[37] for our simulations, which has been updated to the more accurate *R*-matrix collision strength results of version 10 of the CHIANTI database[58]. For each line, we accumulate the emissivities with respect to temperature, denoted by Γ (ref. 31). These are related to the observed line luminosities by $L_{line} = \dot{M}\Gamma$, where $\dot{M}$ is the mass cooling rate.

A pure collisional model led to unphysically high mass cooling rates for all the observed lines. We, therefore, also took into account photoionization by the radiation field of the central AGN, and performed a number of simulations at various distances from the AGN, in the range of 2–20 kpc. To illustrate the gross influence of the AGN, it is worth noting that the gas fails to reach the target temperature, but instead comes into equilibrium with the radiation field at a higher temperature. In more detail, photoionization affects the ionization balance of the gas by driving long ionization tails that extend to much lower temperatures than in the purely collisional case.

How exactly the gas reacts to the AGN radiation depends on how it cools. In isobaric cooling, the effect of photoionization diminishes as the temperature drops because of compression. The gas that contributes to the emissivity of coronal lines, particularly [Ne V] and [Ne VI], covers a much broader temperature range compared with purely collisional cooling, that is, the gas is overionized as it cools to nebular temperatures, and the integrated emissivities of all the coronal lines of interest are boosted. By contrast, in isochoric (constant-density) cooling, the impact of photoionization is more marked. The gas comes to equilibrium with the AGN radiation at higher temperatures than the isobaric case, whereas its effect on integrated emissivities is more complicated, with some enhanced relative to the purely collisional case, and some reduced.

In our final runs, we used a combination of isobaric and isochoric cooling. For a description of these methods and our systematic uncertainty analysis, see the Supplementary Information.

Kinematic models

Here we expand on how the velocity models shown in Fig. 4 are created. Each model has a different inclination angle *i*, which is adjusted to best match the observed profile, such that $v_{los} = v\sin i$.

The solid red line simply gives the circular rotational velocity:

$$v = \sqrt{\frac{GM(r)}{r}}, \quad (2)$$

where $M(r)$ is obtained using a combination of strong lensing and X-ray analyses[20]. The dashed red line gives a ballistic model in which a test particle starts at $r_0 = 6.75$ kpc and $v_0 \sin i = 270$ km s^{-1} and is then enabled to free fall. The blue line gives an ionized wind model driven by supernovae discussed in ref. 59, including the effects of gravity and cooling, and using a star formation rate of 800 $M_\odot$ yr^{-1} (ref. 17), mass loading factor $\eta_M = 0.3$ and a half-opening angle of π/8. The purple line (Fig. 4) gives an outflow model driven by radiation pressure from an AGN, using an analytical model from ref. 60:

$$v(r) = \sqrt{\int_{r_1}^{r} \left[4{,}885 \frac{L_{44}\mathcal{M}}{r^2} - 8.6 \times 10^{-3} \frac{M}{r^2} \right] dr} \quad (3)$$

with a launch radius of $r_1 = 1$ kpc, a bolometric AGN luminosity of $L_{44} = 3{,}000$ ($\times 10^{44}$ erg s^{-1}) (ref. 17) and force multiplier $\mathcal{M} = 500$, which accounts for the increased efficiency of radiative acceleration above that of pure Thomson scattering ($\mathcal{M} = 1$) from bound–bound, bound–free and free–free opacities.

Finally, the bubble model (Fig. 4, green) is obtained by numerically solving a series of differential equations:

$$\frac{\mathrm{d}v}{\mathrm{d}t} = \frac{\rho_{\mathrm{ICM}} V_{\mathrm{b}}}{M_{\mathrm{b}}} \frac{\mathrm{GM}(r)}{r^2} - \frac{1}{2} \frac{\rho_{\mathrm{ICM}}}{M_{\mathrm{b}}} C_{\mathrm{D}} A_{\mathrm{b}} v^2, \tag{4}$$

$$\frac{\mathrm{d}V_{\mathrm{b}}}{\mathrm{d}t} = -\frac{V_{\mathrm{b}}}{\gamma_{\mathrm{ad}} P_{\mathrm{b}}} \frac{\mathrm{d}P_{\mathrm{b}}}{\mathrm{d}t}. \tag{5}$$

Here r is the distance from the nucleus to the centre of the bubble and v is the bubble velocity. The bubble is assumed to be spherical, with V_{b}, P_{b}, A_{b}, M_{b} and R_{b} denoting the volume, pressure, cross-sectional area, mass and radius of the bubble, respectively. $M(r)$ is the enclosed mass of the galaxy at radius r, $\rho_{\mathrm{ICM}} = \mu m_{\mathrm{p}} n_{\mathrm{e}}$ is the density of the ambient ICM, $C_{\mathrm{D}} = 0.5$ is the drag coefficient and $\gamma_{\mathrm{ad}} = 4/3$ is the adiabatic index of the bubble[33]. Equation (4) gives the velocity from the competing effects of the buoyancy force and drag force—the effects of gravity on the entrained mass are not included. Equation (5) gives the rate of expansion of the bubble volume assuming adiabatic expansion. For the pressure $P_{\mathrm{b}}(r)$ and density $\rho_{\mathrm{ICM}}(r)$, we use the one-dimensional pressure and density profiles of the Phoenix cluster ICM obtained from the Chandra observations[23], from which we obtain $\mathrm{d}P_{\mathrm{b}}/\mathrm{d}r$ using a finite difference approximation.

The bubble starts at $r = 0.05$ kpc, whereas our lowest sample for the pressure and density profiles are at 3 kpc, which necessitates extrapolating down to the starting radius of the bubble. The thermodynamics at such small radii are not well constrained, so we take two extreme approaches: (1) assuming the pressure and density are both flat below 3 kpc and (2) extrapolating the pressure and density below 3 kpc with a power law based on the first few data points. The starting parameters of both models are shown in Supplementary Table 2. The initial bubble radius is chosen such that it evolves to the currently observed size of the bubble (approximately 8.5 kpc)[12] when it reaches the currently observed position of the bubble (approximately 20 kpc)[12], and the entrained mass is adjusted to best match the observed velocity profile. Note that further to the uncertainty imparted by the extrapolation of the pressure and density profiles below 3 kpc, the model parameters listed in Supplementary Table 2 have some large degeneracies with each other, particularly mass (M_{b}) or density ($\rho_{\mathrm{b,0}}$) and inclination (i), which affect the overall normalization of the velocity curve. We stress that the purpose of these models is to illustrate the general agreement between the data and the bubble uplift scenario, but a rigorous model capturing the intricate physics expected in the wake of a bubble would be far more complex. As such, we do not attempt to use these models to make any predictions or constraints on the actual amount of cooling coronal gas.

Data availability

Data for JWST programme ID 2439 are publicly available through the Mikulski Archive for Space Telescopes of the Space Telescope Science Institute. Supplementary data used in our analysis from HST are also available through the Mikulski Archive for Space Telescopes. Chandra data are available from the Chandra Data Archive (https://cxc.harvard.edu/cda/).

Code availability

JWST, HST and Chandra data were reduced using the publicly available reduction pipeline codes provided by the Space Telescope Science Institute and Chandra X-ray Center. The Likelihood Optimization of gas Kinematics code used in our analysis is available through GitHub at https://github.com/Michael-Reefe/Loki.jl, and Cloudy is available at https://nublado.org. We also provide our customized driver scripts for data reduction and analysis through GitHub at https://github.com/Michael-Reefe/Reefe2024_code_supplements.

48. Spilker, J. S. et al. Spatial variations in aromatic hydrocarbon emission in a dust-rich galaxy. *Nature* **618**, 708–711 (2023).
49. Bezanson, J., Edelman, A., Karpinski, S. & Shah, V. B. Julia: a fresh approach to numerical computing. *SIAM Rev.* **59**, 65–98 (2017).
50. Smith, J. D. T. et al. The mid-infrared spectrum of star-forming galaxies: global properties of polycyclic aromatic hydrocarbon emission. *Astrophys. J.* **656**, 770–791 (2007).
51. Fitzpatrick, E. L. & Massa, D. An analysis of the shapes of ultraviolet extinction curves. I. The 2,175 angstrom bump. *Astrophys. J.* **307**, 286 (1986).
52. Donnan, F. R. et al. The obscured nucleus and shocked environment of VV 114E revealed by JWST/MIRI spectroscopy. *Mon. Not. R. Astron. Soc.* **519**, 3691–3705 (2023).
53. Labiano, A. et al. Wavelength calibration and resolving power of the JWST MIRI medium resolution spectrometer. *Astron. Astrophys.* **656**, A57 (2021).
54. Tsuchikawa, T. et al. A systematic study of silicate absorption features in heavily obscured AGNs observed by Spitzer/IRS. *Astron. Astrophys.* **651**, A117 (2021).
55. Veilleux, S. et al. Spitzer Quasar and Ulirg Evolution Study (QUEST). IV. Comparison of 1 Jy ultraluminous infrared galaxies with Palomar-Green quasars. *Astrophys. J. Supp.* **182**, 628–666 (2009).
56. Markwardt, C. B. Non-linear least-squares fitting in IDL with MPFIT. in *Astronomical Data Analysis Software and Systems XVIII* (eds Bohlender, D. A. et al.) 251 (2009).
57. Mogensen, P. K. & Riseth, A. N. Optim: a mathematical optimization package for Julia. *J. Open Source Softw.* **3**, 615 (2018).
58. Del Zanna, G., Dere, K. P., Young, P. R. & Landi, E. CHIANTI—an atomic database for emission lines. XVI. version 10, further extensions. *Astrophys. J.* **909**, 38 (2021).
59. Fielding, D. B. & Bryan, G. L. The structure of multiphase galactic winds. *Astrophys. J.* **924**, 82 (2022).
60. Meena, B. et al. Investigating the narrow-line region dynamics in nearby active galaxies. *Astrophys. J.* **943**, 98 (2023).

Acknowledgements This work is based on observations with the NASA/ESA/CSA JWST obtained from the Data Archive at the Space Telescope Science Institute, which is operated by the Association of Universities for Research in Astronomy, Incorporated, under NASA contract number NAS 5-03127. Support for programme number JWST-GO-02439.001-A was provided through a grant from the Space Telescope Science Institute under NASA contract number NAS 5-03127. This work is also based in part on observations made with the NASA/ESA HST obtained from the Space Telescope Science Institute, which is operated by the Association of Universities for Research in Astronomy under NASA contract number NAS 5-26555. These observations are associated with programme number GO15315. Support for this work was also provided by NASA through Chandra award number GO7-18124 issued by Chandra, which is operated by the Smithsonian Astrophysical Observatory for and on behalf of NASA under contract number NAS8-03060. M.R. acknowledges support from the National Science Foundation Graduate Research Fellowship under grant number 2141064. M.G. acknowledges support from the ERC Consolidator Grant BlackHoleWeather (101086804). M. Chatzikos acknowledges support from NSF (1910687) and NASA (19-ATP19-0188 and 22-ADAP22-0139). H.R. acknowledges an Anne McLaren Fellowship from the University of Nottingham. We thank the members of the MIRI/MRS instrument team, particularly D.L., for providing advice and guidance in reducing and cleaning the MIRI/MRS data.

Author contributions M.R. reduced the MIRI/MRS data; wrote and ran the spectral fitting and PSF decomposition code; performed the main analysis of the ionization, kinematics and cooling; and wrote the paper. M.M. provided substantial guidance in the main analyses, interpretation of the results and writing the paper; he also wrote the original proposal for the MIRI/MRS data. M. Chatzikos performed the Cloudy simulations and wrote the description of these processes in Methods. J.S. performed a sanity check on our data reduction and spectral modelling by running an independent pipeline (Q3Dfit). K.S. formulated strong lensing models to estimate the gravitational potential, which we used in our kinematic modelling. R.M., S.V., S.W.A., M.B., M. Calzadilla, R.C., B.F., M.G., J.H.-L., B.M., H.R. and T.S. provided feedback on the paper drafts.

Competing interests The authors declare no competing interests.

Additional information

Supplementary information The online version contains supplementary material available at https://doi.org/10.1038/s41586-024-08369-x.

Correspondence and requests for materials should be addressed to Michael Reefe.

Peer review information *Nature* thanks the anonymous reviewers for their contribution to the peer review of this work. Peer reviewer reports are available.

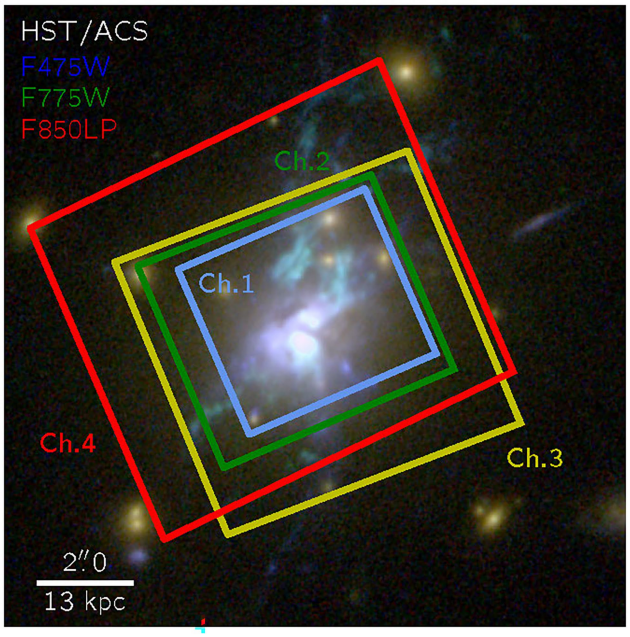

Extended Data Fig. 1 | The field of view of the MIRI/MRS instrument relative to the size of the central galaxy in the Phoenix Cluster. The field of view of each of the four MIRI channels shown over a 3-color image of the core of the Phoenix cluster using data from HST/ACS in the F475W, F775W, and F850LP filters. The dust-obscured AGN lies at the center of the brightest cluster galaxy. The angular and physical scales are annotated in the bottom-left.

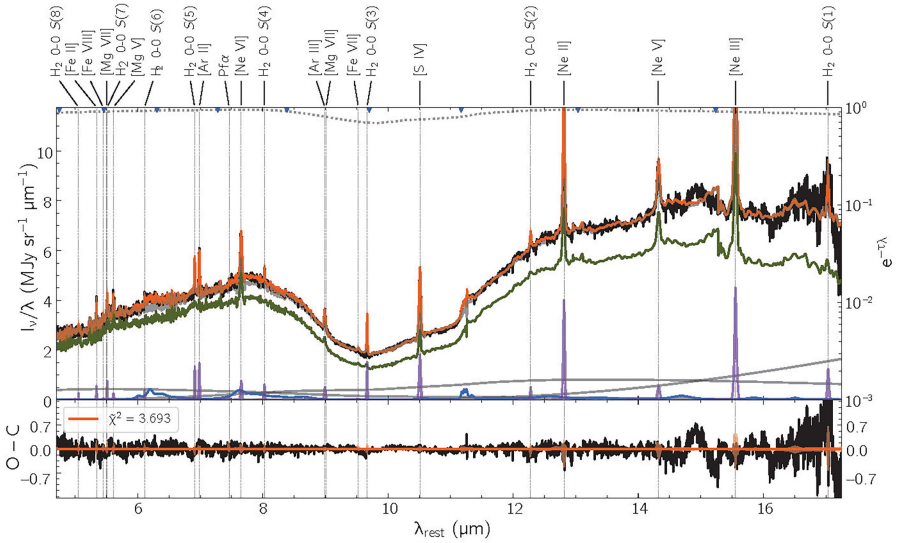

Extended Data Fig. 2 | The full mid-infrared spectrum of the central galaxy in the Phoenix Cluster. A spectrum covering MIRI channels 2–4 (excluding the long wavelength end of 4C), and integrated over the full channel 2 FOV. The top panel shows the data in black and the model in orange, while the bottom panel shows the residuals. The model is also decomposed into components: the gray solid lines are the thermal dust continua, the green line is the QSO PSF model, the blue line is the PAH emission, the purple lines are the emission lines, and the dotted gray line shows the extinction profile. The sum of the thermal dust continua and QSO PSF is also shown by the thick gray line. The emission lines are labeled at the top of the plot, with vertical dashed lines showing their locations in the spectrum. The boundaries between channels and bands are also shown at the top of the plot with blue arrows. The translucent orange region shows the range of models produced in the different bootstrapping iterations.

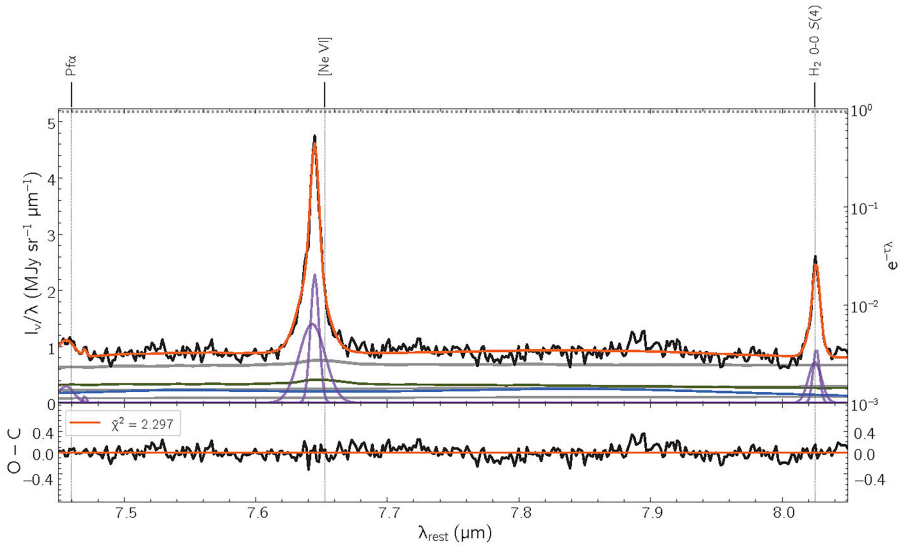

Extended Data Fig. 3 | A zoomed-in emission line spectrum of the central galaxy in the Phoenix Cluster. A subset of the MIRI channel 3 spectrum zoomed in on the [Ne VI] line. This spectrum includes only a single spaxel north of the nucleus. The formatting of everything is identical to Extended Data Fig. 2, except that there is no translucent orange region since this fit has not been bootstrapped. The two distinct kinematic components of the emission lines can be seen in purple.

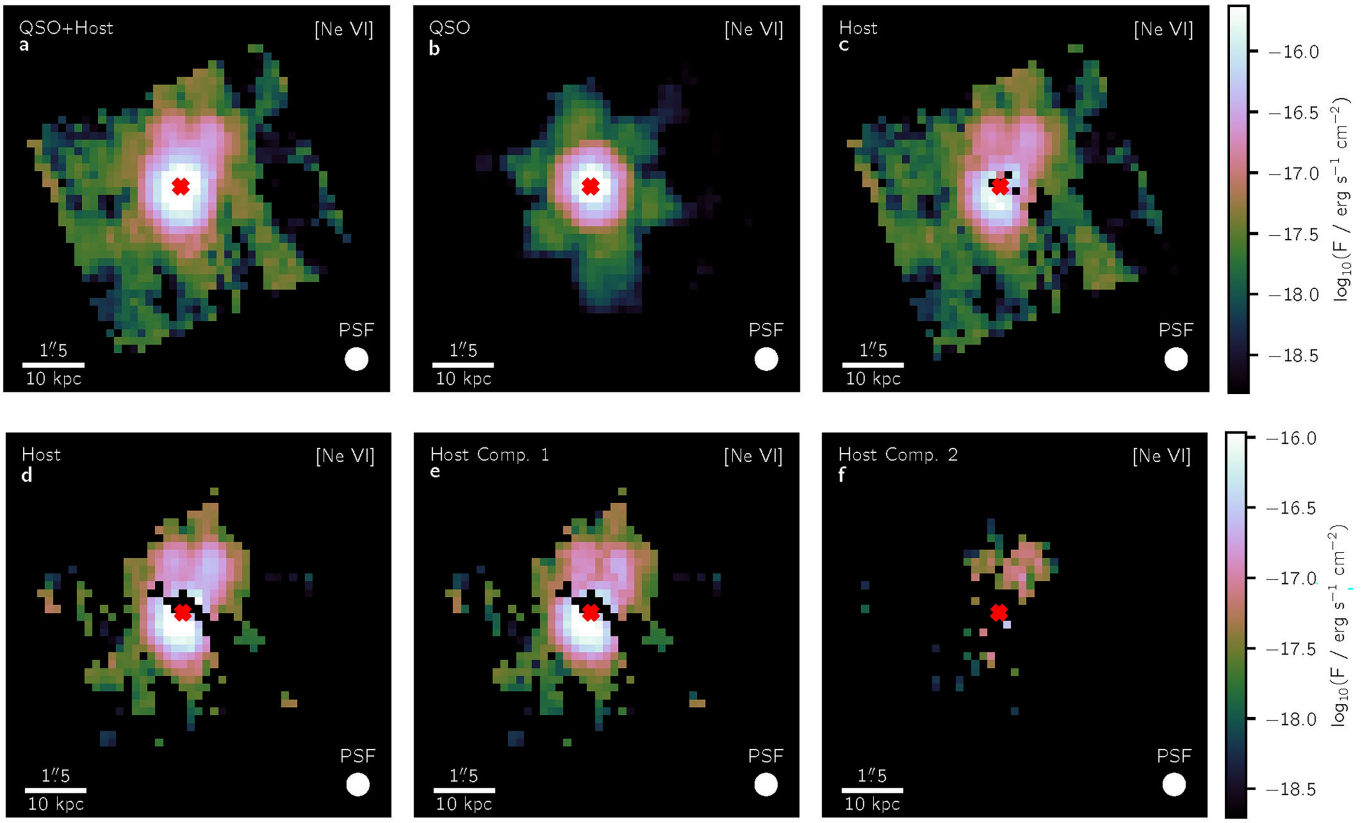

Extended Data Fig. 4 | A series of flux maps for [Ne VI] over the MIRI channel 3 FOV showing the decomposition into various spatial and kinematic components. a-c show the QSO and host galaxy components of the flux. **a**, the total observed flux, **b**, the flux from the QSO that has been dispersed according to the PSF model, and **c**, the QSO-subtracted flux that is attributed to the host galaxy. **d-f** show the further decomposition of the host galaxy flux into 2 distinct kinematic components, now with an *S/N* cut such that only spaxels with a detection of $S/N \geq 3$ are shown. **d**, the combined flux from both kinematic components, making it identical to **c** except for the SNR cut. **e** and **f**, the fluxes from each individual kinematic component, sorted in order of decreasing flux. The color scales are shown on the right of each row and are the same for each panel in that row. The physical scale in kpc and angular scale in arcsec are annotated in the bottom left of each panel, and the FWHM of the PSF at the wavelength of [Ne VI] is shown in the bottom right of each panel.

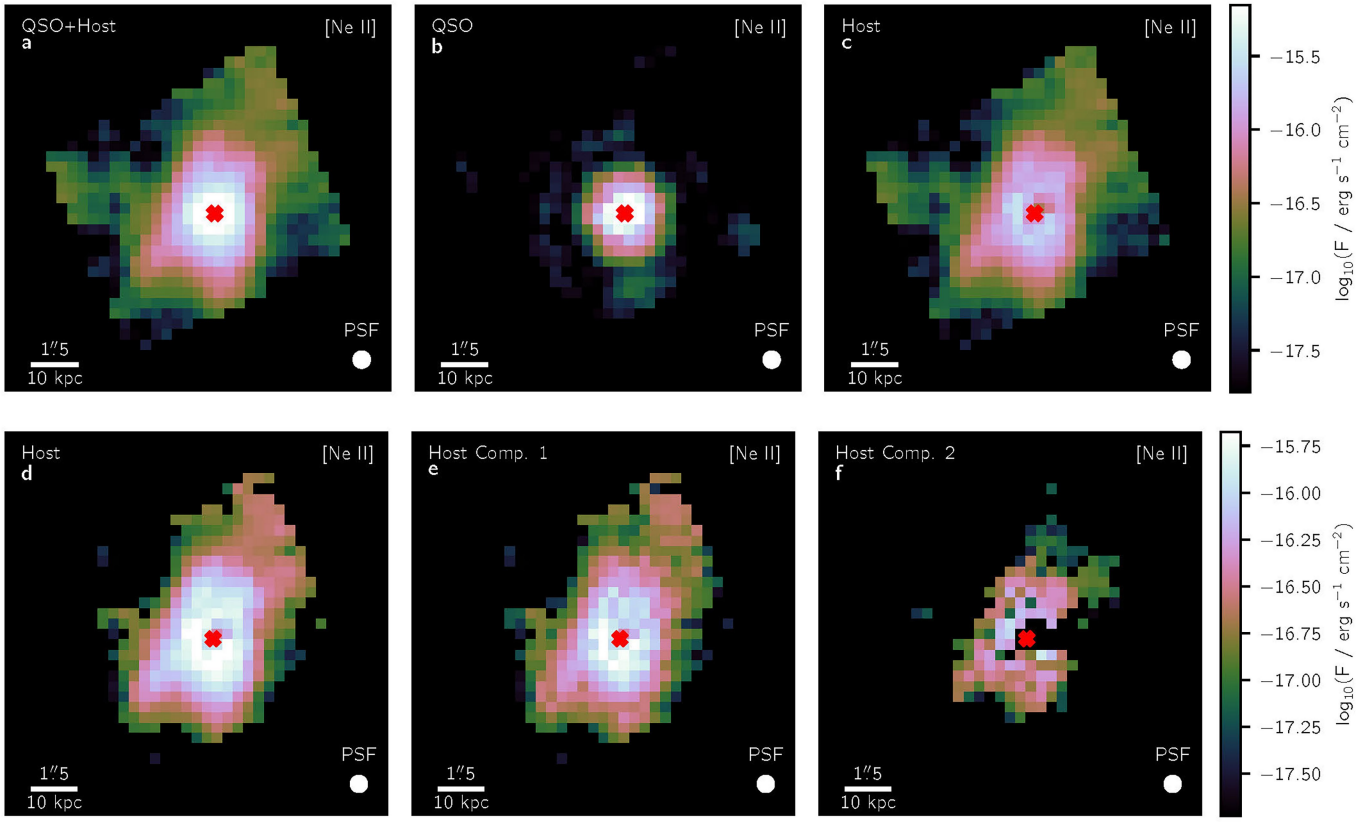

Extended Data Fig. 5 | A series of flux maps for [Ne II] over the MIRI channel 4 FOV showing the decomposition into various spatial and kinematic components. Same as Extended Data Fig. 4, but for [Ne II] λ12.813 μm.

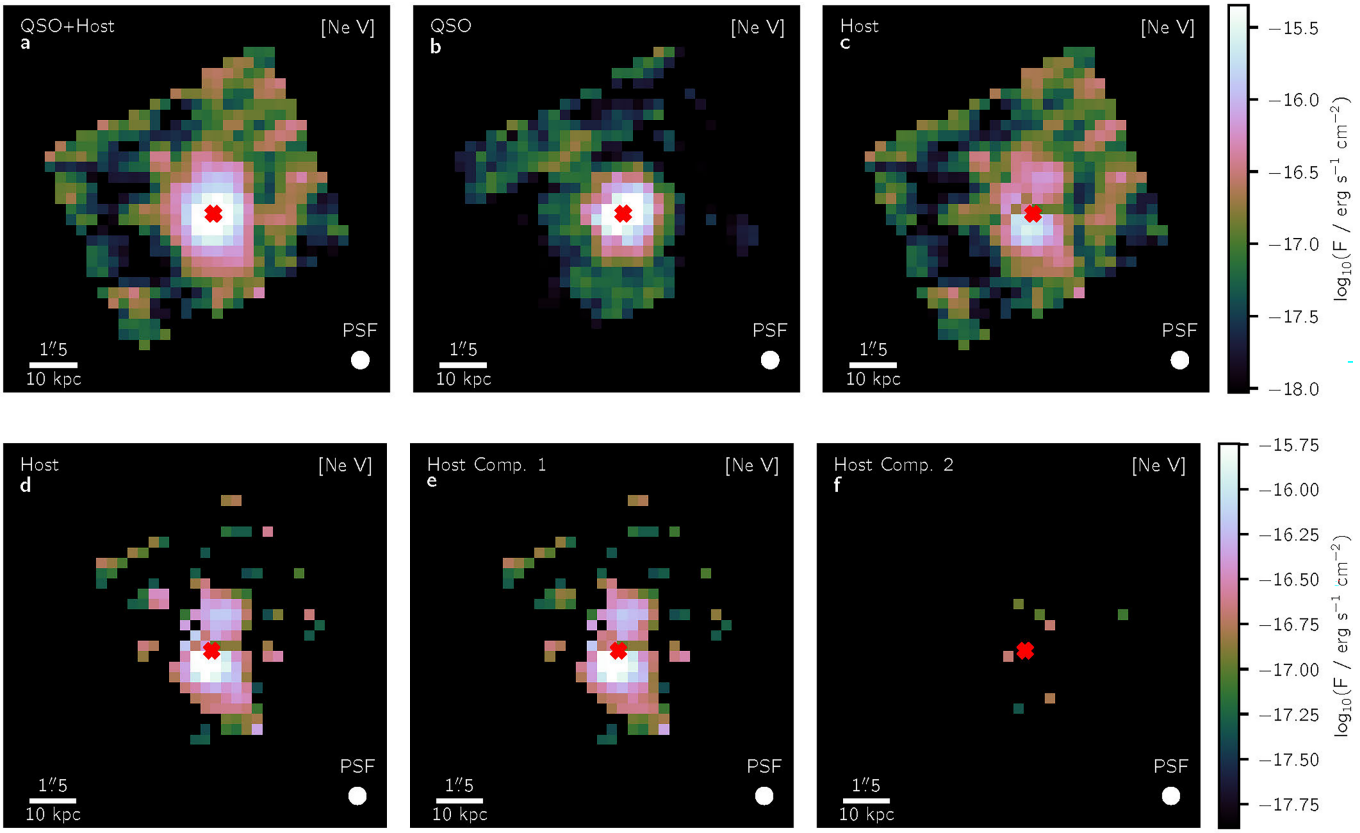

Extended Data Fig. 6 | A series of maps for [Ne v] over the MIRI channel 4 FOV showing the decomposition into various spatial and kinematic components. Same as Extended Data Fig. 4, but for [Ne v] λ14.322 μm.

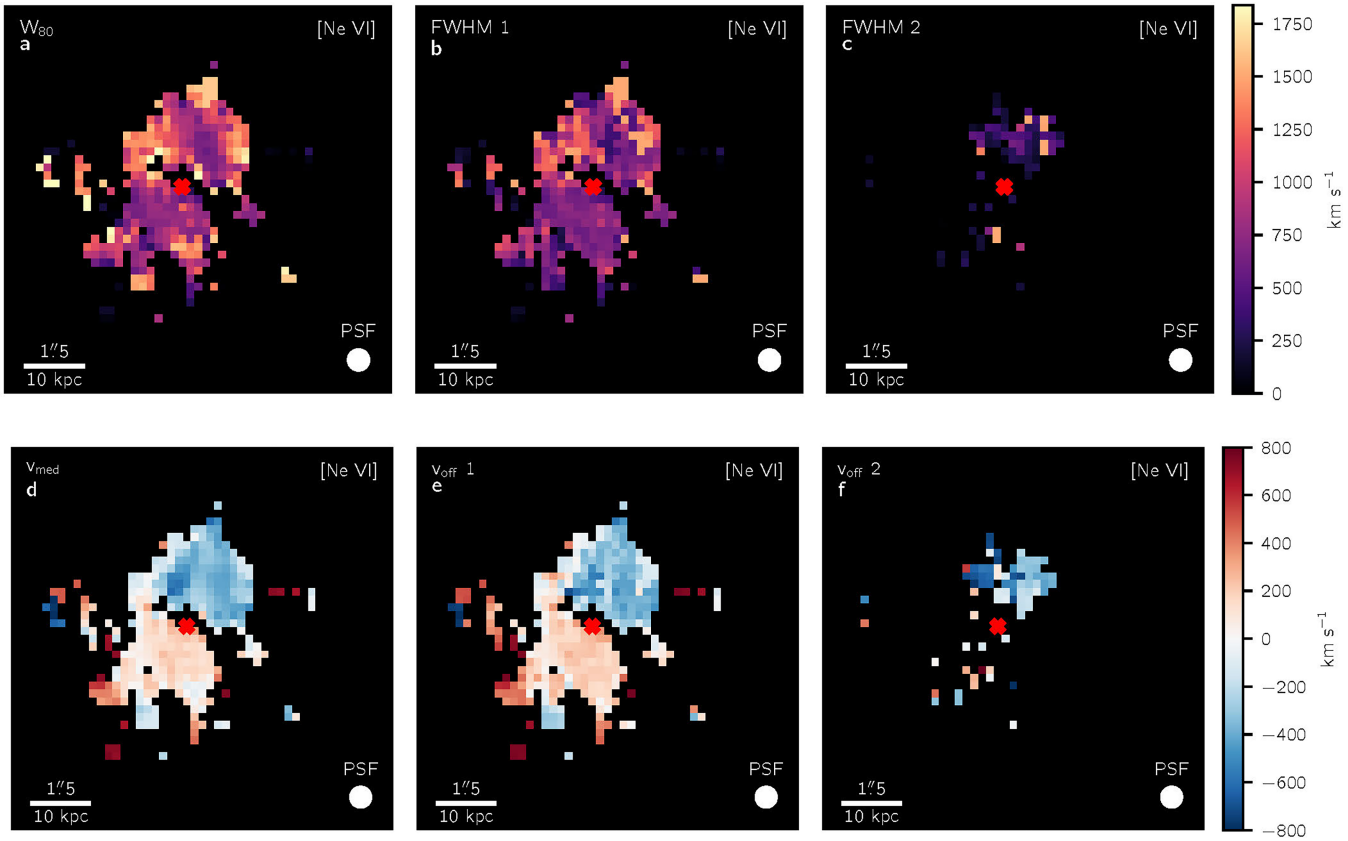

Extended Data Fig. 7 | A series of kinematic maps for [Ne VI] over the MIRI channel 3 FOV showing the decomposition into various kinematic components. **a**-**c** show the line velocity widths. **a**, the W_{80} of the full line profile, **b** and **c**, the FWHMs of the individual kinematic components. **d**-**f** show the LOS velocities. **d**, the median LOS velocity of the full line profile, **e** and **f**, the peak velocities of the individual kinematic components. All maps have an $S/N \geq 3$ cut. The color scales are shown on the right of each row and are the same for each panel in that row. The physical scale in kpc and angular scale in arcsec are annotated in the bottom left of each panel, and the FWHM of the PSF at the wavelength of [Ne VI] is shown in the bottom right of each panel.

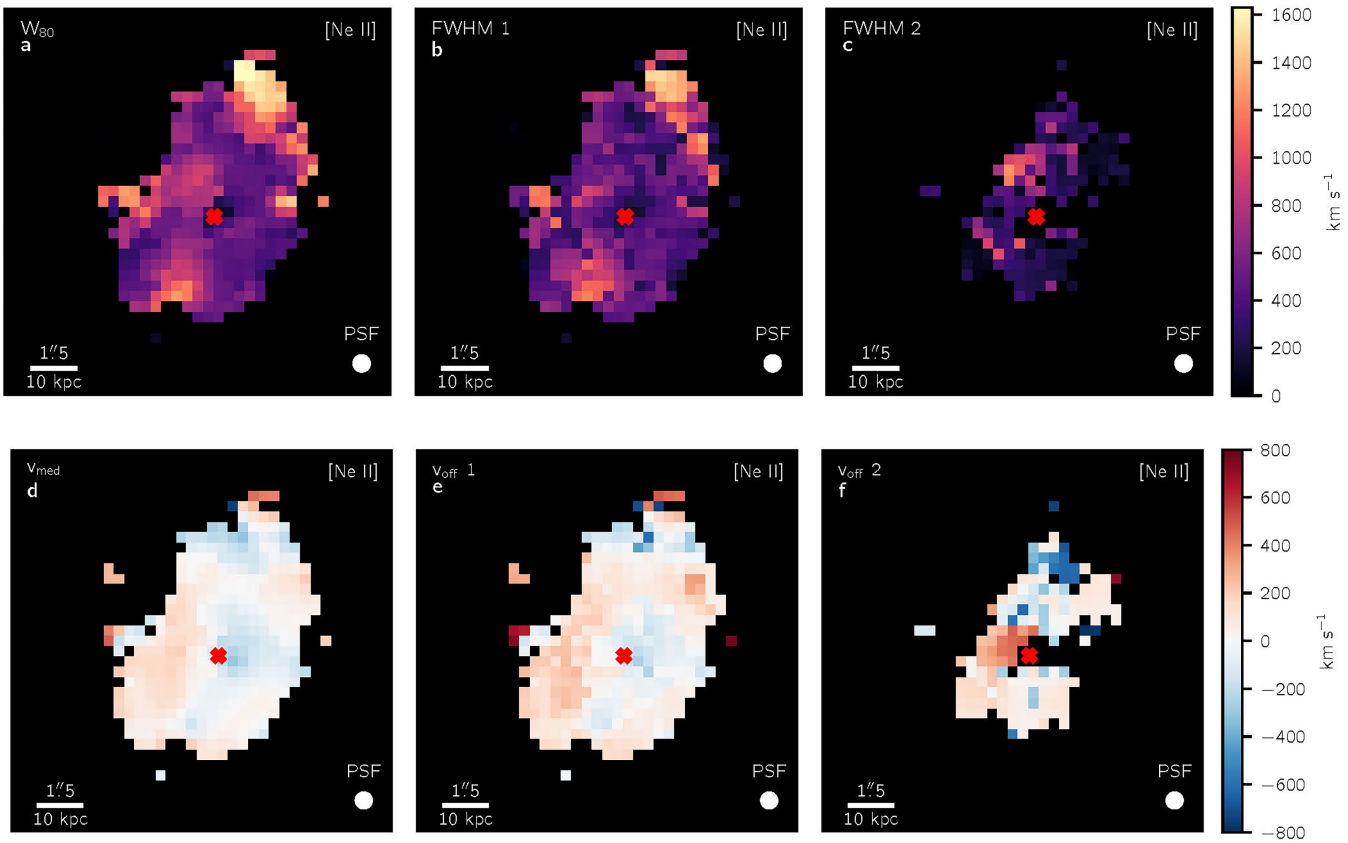

Extended Data Fig. 8 | A series of kinematic maps for [Ne II] over the MIRI channel 4 FOV showing the decomposition into various kinematic components. Same as Extended Data Fig. 7, but for [Ne II] λ12.813 μm.

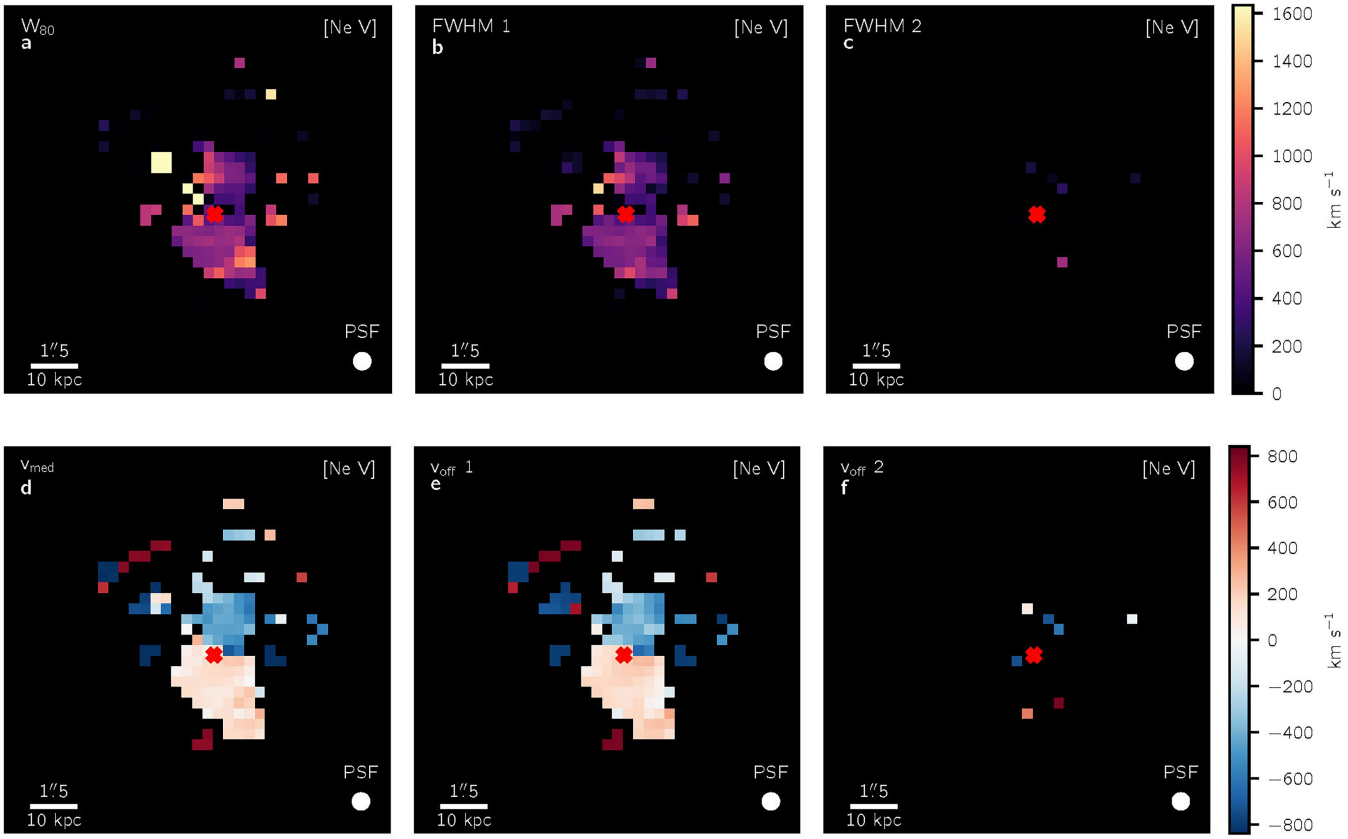

Extended Data Fig. 9 | A series of kinematic maps for [Ne v] over the MIRI channel 4 FOV showing the decomposition into various kinematic components. Same as Extended Data Fig. 7, but for [Ne v] λ14.322 μm.

Extended Data Table 1 | Emission line fluxes in various regions

Line	λ (vacuum) μm	IP* eV	F_{north}† erg s^{-1} cm^{-2} $\times 10^{-16}$	$F_{nucleus}$‡ erg s^{-1} cm^{-2} $\times 10^{-15}$	F_{host}§ erg s^{-1} cm^{-2} $\times 10^{-15}$
[Fe VIII]	5.4466	124.97	0.3 ± 0.1	$2.1^{+0.5}_{-0.6}$	0.4 ± 0.2
[Mg VII]	5.5032	186.76	0.9 ± 0.1	2.0 ± 0.3	0.7 ± 0.3
[Mg V]	5.6099	109.27	1.2 ± 0.3	$3.6^{+0.2}_{-0.5}$	$1.5^{+0.3}_{-0.2}$
[Ne VI]	7.6524	126.25	$4.9^{+0.5}_{-0.7}$	12^{+1}_{-2}	$4.3^{+0.3}_{-0.4}$
[Mg VII]	9.0090	186.76	0.9 ± 0.2	$0.2^{+0.3}_{-0.2}$	< 0.5‖
[Fe VII]	9.5267	98.99	$0.4^{+0.2}_{-0.1}$	$2.5^{+0.4}_{-0.5}$	$0.3^{+0.2}_{-0.1}$
[S IV]	10.5105	34.86	18.6 ± 0.6	$25.5^{+0.4}_{-0.1}$	$12.4^{+0.8}_{-0.7}$
[Ne II]	12.8136	21.56	18 ± 2	17 ± 1	15 ± 5
[Ne V]	14.3217	97.19	5 ± 1	11 ± 1	3.3 ± 0.6

*The ionization energy required to create ions of the given species, obtained from NIST.

†The integrated flux within an elliptical aperture covering the region of extended emission to the north of the nucleus, with the QSO contribution subtracted.

‡The integrated flux within a circular aperture with a 1″ radius centered on the nucleus, including the QSO contribution.

§The integrated flux throughout the full channel 2 FOV, with the QSO contribution subtracted.

‖3σ upper limits are derived by integrating a gaussian with an amplitude of 3 times the continuum RMS at the location of the line, with a width of 1000 km s^{-1}.